

High-Frequency/High-Field Electron Spin Echo Envelope Modulation Study of Nitrogen Hyperfine and Quadrupole Interactions on a Disordered Powder Sample

A. Bloëß,¹ K. Möbius, and T. F. Prisner^{2,3}

Freie Universität Berlin, Arnimallee 14, D-14195 Berlin, Germany

Received December 30, 1997; revised April 7, 1998

High-frequency/high-field (95 GHz/3.4 T) electron spin echo envelope modulation (ESEEM) experiments on single crystals and disordered samples of dianisyl-nitroxide (DANO) radicals are reported. At these high microwave frequencies (W-band), the anisotropic g -matrix of the nitroxide radical is resolved in the EPR spectrum. Additionally ESEEM modulations from other than nitrogen nuclei, such as protons, are highly suppressed at these frequencies, because they are too far from the cancellation condition for effective mixing of the nuclear spin functions. Therefore the nitrogen (^{14}N) hyperfine and quadrupole coupling tensors could be determined without ambiguity from powder measurements. The results obtained were checked by ESEEM measurements on single crystals. Advantages and disadvantages of high-field ESEEM on nitrogen couplings are briefly discussed and compared with electron nuclear double resonance (ENDOR) and X-band ESEEM. © 1998 Academic Press

Key Words: high-field EPR; high-frequency EPR; ESEEM; pulse EPR; nitrogen hyperfine coupling.

INTRODUCTION

Direct information on the structure of paramagnetic molecules and their environment are provided by spin coupling parameters from hyperfine and quadrupole interactions of the unpaired electron spin with nuclei of the molecule and the surrounding matrix. Advanced electron paramagnetic resonance (EPR) techniques, such as ENDOR and ESEEM, have proven to be powerful tools in extracting such information (1–5). For a detailed structure determination the knowledge of all interaction tensors of the spin Hamiltonian is often necessary. Complete coupling tensors can be obtained best from single-crystal measurements, which allow one to examine different molecular orientations (and thereby different elements of the tensors) separately. However, growing of sufficiently large single crystals is not trivial and for many biological systems

still not possible. Moreover the paramagnetic centers in the crystal often exist in different sites, leading to complications in the spectra and ambiguities in the analysis. Usually the situation is even worse for powders. All orientations are present simultaneously with overlapping spectra and hence hyperfine splittings are normally covered under a broad inhomogeneous lineshape. The situation is especially complicated when the g -matrix anisotropy is comparable to or smaller than the hyperfine splittings involved, as is often the case at X-band frequencies (9 GHz/0.3 T). The difficulties can be overcome by going to higher-field/frequency values, where the anisotropy of the g -matrix becomes well resolved in the EPR spectrum. Thus, by means of the higher field, one achieves a separation of the different molecular orientations with respect to the field axis. A typical example of such a magnetoselection by the Zeeman field is given by nitroxide radicals at W-band (95 GHz/3.4 T), where the main molecular orientations can be clearly distinguished by the g -matrix principal values in the spectrum (6–8).

In nitroxide radicals the large nitrogen hyperfine coupling A_{zz} can often be directly obtained from the EPR spectrum, whereas the small hyperfine components A_{xx} and A_{yy} are hidden under the inhomogeneous linewidth. In this case the combination of high spectral resolution achieved by high-field EPR with a technique sensitive to small nuclear couplings, such as ESEEM or ENDOR, can lead to the missing hyperfine and quadrupole information. Both techniques add a second dimension to the experiment (a radiofrequency (RF) dimension in the ENDOR experiment, a time dimension in the ESEEM experiment), increasing the spectral resolution further by suppressing the inhomogeneous broadening in this second dimension. Due to the narrow excitation width of the applied microwave (mw) pulses, holes are burned into the inhomogeneously broadened EPR line. Therefore, for a specific field value only molecules with the appropriate g -value for the resonance condition are selected. The frequencies showing up in ESEEM or ENDOR spectra can consequently be directly attributed to corresponding molecular orientations. As a result the disadvantage of unstructured powder EPR spectra is partly overcome and crystal-like information can be gained. How many orien-

¹ Present address: Huygens Laboratory, Leiden University, The Netherlands.

² Present address: Institut für Physikalische und Theoretische Chemie, JW Goethe-Universität, Marie-Curie-Str. 11, D-60439 Frankfurt am Main, Germany.

³ To whom correspondence should be addressed.

tations are simultaneously excited depends on the ratio between spectral width and excitation width, which, in our case, is 50 (150 and 3 G, respectively).

In order to obtain substantial echo modulation intensities one has to meet the requirement that the Zeeman splitting of the nuclear sublevels be approximately half of the respective hyperfine coupling for $I = 1$ (cancellation condition). In this case the nuclear spin eigenfunctions will be mixed efficiently by the dipolar interaction with the electron spin (differently for both electronic spin quantum states, $m_s = +\frac{1}{2}$ and $-\frac{1}{2}$). Consequently an optimum Zeeman field value exists for each hyperfine coupling for a maximum modulation depth. This requirement has been examined in detail at mw frequencies in the range of 8–12 GHz (9). Different nuclei give rise to the ESEEM effect at different mw frequencies, and the mw frequency has to be chosen carefully to optimize both spectral resolution and ESEEM detection sensitivity. In addition to the increased resolution in the spectral range, there is another advantage of performing two-dimensional experiments at higher external magnetic field values (and respective mw frequencies): the increased spectral resolution in the nuclear frequency dimension. Hyperfine lines of different nuclei (e.g., ^1H , ^{15}N , ^{31}P , ^{17}O) will be well separated by their different Larmor frequencies. At X-band, hyperfine lines of these nuclei often show up within the same RF frequency range. This additionally complicates the spectrum analysis and makes more complex and time consuming experiments necessary (10, 11).

Pulsed ENDOR experiments, on the other hand, are not restricted by the cancellation condition, but also depend on the spin relaxation times T_1^e , T_1^n and, to some extent, on T_2^e . The respective pulse lengths for the RF π pulse and the pulse separations τ and T of the mw pulses have to be short compared to the relaxation times. For nuclei with small gyromagnetic ratios (such as ^2H or ^{14}N) the optimum RF pulse lengths easily become longer than 20 μs , and thus exceed typical electron relaxation times at room temperature. This could be the reason why so far we were not able to record ^{14}N ENDOR spectra of this nitroxide radical at temperatures above 110 K (T_1^e is 80 μs at 110 K and 4 μs at RT). Obviously, both methods, ESEEM and ENDOR, have their advantages and disadvantages, and additional criteria have to be considered when going to higher microwave frequencies. It is the purpose of this paper to demonstrate the feasibility of nitrogen ESEEM even on disordered samples at high magnetic fields. W-band nitrogen ESEEM for single-crystal samples has recently been reported by several groups (12–15).

MATERIALS AND METHODS

All the experiments have been performed with our home-built pulsed 95 GHz/3.4 T EPR/ENDOR spectrometer (14). The pulsed microwave bridge is operating in heterodyne mode with a 95 GHz klystron as the excitation source and a 4 GHz dielectric resonator oscillator as the intermediate frequency source. The probe head (16) consists of a cylindrical, frequency

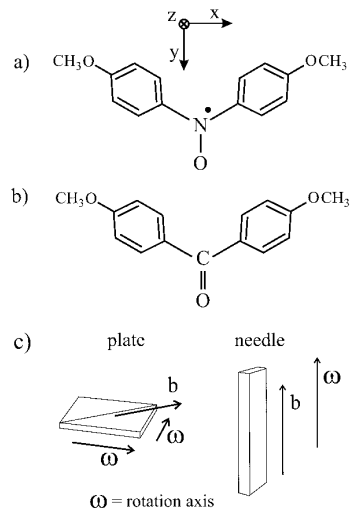


FIG. 1. (a) Nitroxide radical DANO (dianisyl-nitroxide). (b) Dimethoxy-benzophenone host for the diluted DANO crystals. (c) Orientation of the crystal lattice b -axis and the axis of rotation (ω -axis) for the plate and needle crystals, respectively. In the case of the plate crystals, cutting along one of the edges can result in two indistinguishable rotation axes.

tunable TE_{011} microwave resonator inside the warm bore of the superconducting magnet. For this configuration only a one-axis rotation of the sample can be performed. The cavity has a Q -factor of approximately 1000, which limits the bandwidth of the spectrometer to a value of 100 MHz. This is much more than the pulse excitation bandwidth of about 10 MHz, which is limited by the mw power at the cavity (10 mW maximum), the quality factor Q , and the conversion factor of the cavity. The deadtime of the receiver after the microwave pulses is less than 5 ns.

Dianisyl-nitroxide (DANO), a stable nitroxide radical, in which the free electron spin is in close proximity to the nitrogen nucleus (Fig. 1a), serves as our test system for the examination of conditions for detecting hyperfine couplings at W-band frequencies (16). DANO can be crystallized as a low concentration guest in dimethoxy-benzophenone as host material, which has a very similar structure (Fig. 1b). The DANO molecule substitutes in two different sites of the host crystal, which differ by 14° in their orientation (17). In addition, depending on the concentration of DANO, crystallization results in different crystal structures. In order to orient DANO in the magnetic field, one has to know the relative orientation of the molecular axis system (x, y, z) with respect to the crystal lattice axis system (a, b, c) and relative to the morphology of the crystal. The z -axes of the two sites are tilted against the b -axis by $\pm 7^\circ$. The more diluted crystals with a needle-like shape have the b -axis parallel to the long axis of the needle. The more concentrated crystals form flat rhombic plates, with their the b -axis aligned along one of the diagonals of the plates (Fig. 1c).

In this paper we will always refer to the molecular axis system (x, y, z). The g -matrix (\tilde{g}), the nitrogen hyperfine tensor (\tilde{A}), and the quadrupole tensor (\tilde{Q}) are all three collinear for

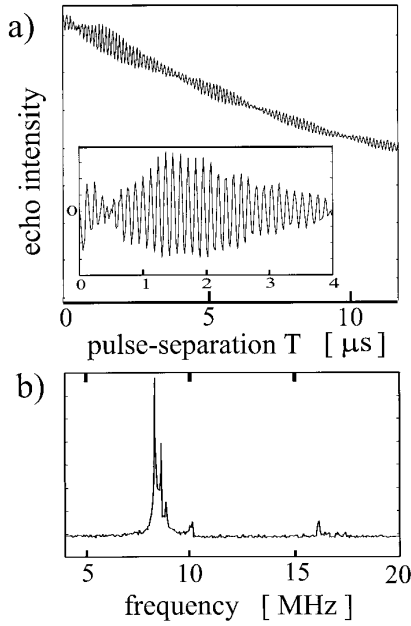


FIG. 2. (a) Three-pulse stimulated echo decay function measured for a DANO crystal. Experimental parameters: microwave pulse length, $t_p = 100$ ns; pulse spacing, $\tau = 260$ ns; pulse separation T between the second and third pulses is stepped in 20 ns increments; 300 echo signals are averaged for each data point in the time domain. The insert shows the echo modulation of the first 4 μ s of the decay function after high-pass filtering. (b) Corresponding ESEEM frequency spectrum after Fourier transformation with a Nyquist frequency of 25 MHz.

symmetry reasons (17), and diagonal in this representation. We had to use both types of crystals, plate and needle, in order to perform two independent rotations in the Zeeman field, because the crystal sizes were too small to cut one of them into perpendicular orientations. While the z -direction is well defined for the needles, this is not the case for the plates. The powder measurements were performed on a polycrystalline DANO sample.

Two-pulse ($2\pi/3 - \tau - 2\pi/3$) as well as three-pulse ($\pi/2 - \tau - \pi/2 - T - \pi/2$) echo decay functions were measured. All measurements were performed at room temperature. Typical pulse lengths after optimizing the echo intensity were between 70 and 100 ns. Because the relaxation of the nuclear coherences was much slower than that of the electronic coherences in stimulated (3-pulse) echo experiments considerably longer echo decay times and thereby much higher frequency resolution were obtained. The possible τ -suppression effect in three-pulse experiments (“blind spots”) was taken care of by recording spectra at different τ values, but no strong amplitude effects were observed. Figure 2 shows a three-pulse echo decay measurement on a DANO crystal. Each measurement point is the average of 300 integrated echo signals for a fixed pulse separation T . The integration window is set to a narrow time interval around the echo maximum to avoid complications of the ESEEM effect seen in the wings of the echo (18). The pulse separation is incremented by 20 ns steps over a total range of 30 μ s. The experiment repetition time is limited by the aver-

aging rate of the transient recorder to 200 Hz. This leads to a total measurement time of approximately 50 min.

In the stimulated echo experiments the echo modulation could be observed for T values up to 15 μ s. The insert in Fig.2a shows the echo modulation signal after high-pass filtering (butterworth filter with cutoff frequency 1 MHz) of the echo decay function. Fourier transformation of this filtered signal gives the ESEEM frequency spectrum in Fig.2b. The width of the nitrogen hyperfine lines is of the order of 0.3 MHz. In the best case the modulation depth was 16% (specific orientation of the single crystal) and modulation frequencies up to 16 MHz could be observed.

THEORY

Simulations of the crystal as well as of the powder ESEEM measurements are based on the mathematical model of Mims (19). The starting point for the calculations is the spin Hamiltonian \hat{H} for one electron spin $S = \frac{1}{2}$ and one nuclear spin $I = 1$ of the nitrogen:

$$\hat{H} = \mu_B \hat{S} \tilde{g} \vec{B} + \hat{S} \tilde{A} \hat{I} - g_N \mu_N \hat{I}_z B_0 + \hat{I} \tilde{Q} \hat{I}. \quad [1]$$

The quadrupole tensor \tilde{Q} in this expression is

$$\tilde{Q} = \begin{pmatrix} Q_{zz}/2 & 0 & 0 \\ 0 & Q_{zz}/2 & 0 \\ 0 & 0 & -Q_{zz} \end{pmatrix}. \quad [2]$$

Instead of describing the experiment in the full density-matrix formalism, usually two important assumptions are made to reduce the complexity of the situation. First, the high-field approximation is used for the electron spin eigenfunctions, and second, the pulses are treated as ideal δ -pulses.

The high-field approximation means that the energy splitting of the electron spin levels is considered to be large enough that direct mixing of the electron spin wavefunctions by hyperfine interaction can be neglected. In mathematical terms this means that only the \hat{S}_z component of the electron spin operator is retained. This has two consequences, namely a decoupling of the six-dimensional problem into the two $m_s = +\frac{1}{2}$ and $m_s = -\frac{1}{2}$ subspaces and, more important, the time dependent Hamiltonian, including the term \hat{H} of Eq. [1] and the microwave contribution \hat{H}_{MW} , can be made time independent by means of a simple transformation into the rotating frame providing the Hamiltonian \hat{H}_{rot} :

$$\hat{H}_{rot} = \hat{H}' + \hbar \omega_1 \hat{S}_x, \quad [3]$$

$$\begin{aligned} \hat{H}' = & \hbar(\omega_s - \omega) \hat{S}_z - g_N \mu_N \hat{I}_z B_0 + \hat{I} \tilde{Q} \hat{I} \\ & + A_{zx} \hat{S}_z \hat{I}_x + A_{zy} \hat{S}_z \hat{I}_y + A_{zz} \hat{S}_z \hat{I}_z. \end{aligned} \quad [4]$$

The second assumption of ideal pulses allows one to neglect the

term \hat{H}' in Eq. [3] for the duration of the pulses. With these approximations the entire problem can be explicitly solved (20). The remaining problem is a diagonalization of \hat{H}' to obtain the eigenvalues and eigenstates for each orientation. ESEEM frequencies are then given by the differences in energy of the nuclear sublevels in each m_s subspace and their intensities are determined by the various transition matrix elements involved.

While the first assumption is well fulfilled already at X -band frequencies (and therefore will apply even better at W -band frequencies), the second condition is not met by the experimental situation at all. In the case of the DANO crystals the only consequence should be that frequencies over 10 MHz are strongly suppressed in the experimental spectrum because of limited B_1 coverage. For powder samples the situation is more complicated. For achieving orientational selection in the spectral dimension, as explained above, the excitation width of the microwave pulses has to be small compared to the spectral width. On the other hand the pulses have to be strong enough to cover the hyperfine frequencies. In this case, the calculations based on the analytical expressions for δ -function microwave pulses will no longer describe the intensities correctly. Thus, since even the 2D powder ESEEM spectrum still consist of many overlapping contributions, the shapes of the lines will strongly depend upon the various intensities. This makes a quantitative spectral simulation more difficult. As a simple approach we calculated the 2D powder ESEEM spectra by continuing to use the δ -function expressions in the ESEEM frequency dimension, but only selecting molecules on-resonance with the microwave frequency in the magnetic field dimension. Effects of finite pulse excitation width were simulated by a convolution of the 2D spectra in the field dimension with the pulse excitation profile.

RESULTS AND DISCUSSION

Powder Measurements

The results of the powder sample measurements are represented in Fig. 3. In Fig. 3a, a two-pulse echo detected field swept EPR spectrum is shown. The three main g values (g_{xx} , g_{yy} , and g_{zz}) are clearly resolved. The field range in which ESEEM frequencies show up at W -band experiments is shaded in gray. The corresponding ESEEM frequencies are shown in a contour plot in Fig. 3b. This 2D spectrum was obtained by recording echo decays at subsequent field positions. Plotted are the high pass-filtered and Fourier transformed echo decays (ordinate) versus the magnetic field value (abscissa).

Surprisingly the ESEEM frequencies observed in the DANO powder sample exhibit little field dependence (Fig. 3b). In fact just one dominant line appears over the entire range of x - and y -orientations, disappearing very quickly as one leaves the spectral range of the xy -plane. No splitting and only a weak field dependence of the ESEEM frequency occurs.

Nevertheless, this line indeed gives specific information about the ^{14}N hyperfine and quadrupole tensor. For the simu-

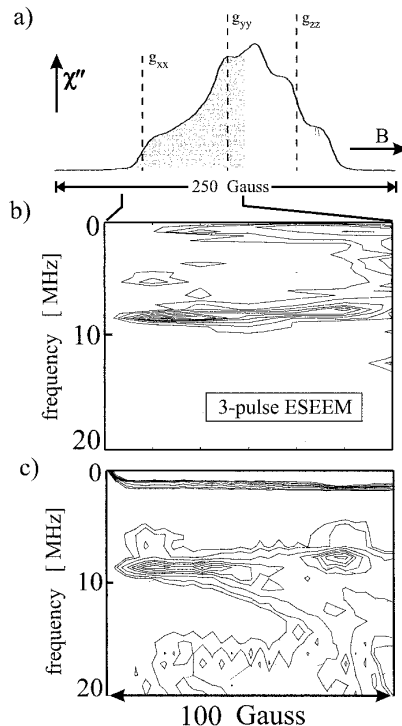


FIG. 3. (a) Two-pulse echo detected field swept EPR spectrum of a DANO powder sample at 95 GHz. The pulse lengths are 85 ns and the pulse spacing τ is 285 ns; 200 echo signals are averaged for each data point in the time domain; gray shading indicates the spectral range where ESEEM frequencies become observable. (b) Frequency-field dependence of three-pulse stimulated echo ESEEM of a DANO powder sample at 95 GHz. Pulse lengths are 75 ns; the pulse spacing τ is 145 ns; the pulse separation T is stepped in 20 ns increments; 400 echo signals are averaged for each data point in the time domain. The contour lines are drawn at equidistant high levels from 0.1 to 1 of maximum FT ESEEM intensity. (c) Simulated three-pulse ESEEM powder spectrum of DANO at 95 GHz. Parameter setting for this simulation: $A_{xx} = 7.4$ MHz, $A_{yy} = 9$ MHz, $A_{zz} = 70$ MHz, $Q_{zz} = 3$ MHz, g -values as given in Table 1.

lation of the powder ESEEM spectrum a number of parameters, namely the largest hyperfine component A_{zz} and the g -matrix main values g_{xx} , g_{yy} and g_{zz} , were previously known and fixed. All of them are well resolved and determined from the 95 GHz EPR spectrum (Fig. 3a). In addition the g -matrix and the hyperfine and quadrupole tensors are assumed to be collinear as explained above and the quadrupole tensor was taken as rhombic. This explains some of the features showing up in the ESEEM powder spectrum, for instance, the sudden disappearance of the ESEEM intensities outside the xy -plane (Fig. 3b). With 70 MHz coupling A_{zz} is too large compared to the ^{14}N Zeeman splitting of 10 MHz at 95 GHz to be excited in the ESEEM experiment. The values of A_{xx} and A_{yy} are both below 15 MHz, which is evident from the linewidth in the crystal EPR spectra. Therefore, leaving the xy -plane quickly leads to conditions far from the cancellation optimum.

As can be seen from a comparison of the simulated with the experimental powder spectrum in Figs. 3b and 3c, the simulation reproduces the experimental intensities very well. This is somewhat surprising in view of the oversimplified model used

for the powder simulation (see above) and since the calculations fit the measured intensities for the crystal rotation patterns much less accurately.

The powder simulation shown in Fig. 3c consists of 14,200 equally distributed orientations. The two-dimensional array is convoluted with a Gaussian function in both directions to take into account finite excitation width and limited modulation lifetime, respectively. The excitation profile in the frequency dimension is described by a simple step function that cut off all frequencies above 20 MHz. Only a unique set of parameter values (A_{xx} , A_{yy} and Q_{zz}) could produce a satisfactory simulation as shown in Fig. 3c, where all the characteristic features of the experimental data array are present: the dominating line (~ 8 MHz) and its field dependence, the small satellites (~ 5 MHz) for the g_{xx} -position, and the broad frequency distribution around the g_{yy} -position. Intensities are also visible in the simulation at frequencies higher than 10 MHz. But they could hardly be detected in the experiment because of the lack of B_1 coverage. The values determined for the hyperfine components A_{xx} and A_{yy} and the quadrupole main value Q_{zz} are listed in Table 1. The hyperfine values A_{xx} and A_{yy} determined by our W-band ESEEM experiment differ substantially from those extracted from previous continuous wave (cw) X-band work on single crystals (17). This is probably due to limited resolution of the different sites in the cw X-band spectra. The quadrupole splitting could not be determined by these experiments.

Single-Crystal Measurements

Typical ESEEM spectra obtained for the DANO crystal samples are shown in Fig. 2b. As can be seen also from the rotation patterns in Fig. 4, the lines cannot easily be assigned to the quadrupole split ^{14}N transitions of the two sites. Furthermore, the expected sinusoidal shift of the hyperfine frequency with crystal rotation is strongly distorted by the quadrupole coupling and, in addition, the sum rule applying for transitions of one nuclear subspace is not found back in the measured ESEEM frequencies. The computer program used for the simulation of the rotation patterns is basically the same as that described earlier for the powder spectrum simulations.

TABLE 1

The g -Matrix Components and ^{14}N Hyperfine and Quadrupole Couplings (in MHz) as Determined from the W-Band Measurements (EPR and ESEEM Spectra of Powder and Single-Crystal Samples)

	Powder EPR	Powder ESEEM	Crystal ESEEM
g_{xx}	2.0091(1)		
g_{yy}	2.0053(1)		
g_{zz}	2.0023(1)		
A_{zz}	69.7(6)		
A_{xx}		7.0(1.0)	7.6(3)
A_{yy}		8.5(1.0)	9.0(1)
Q_{zz}		2.5(1.0)	3.0(1)

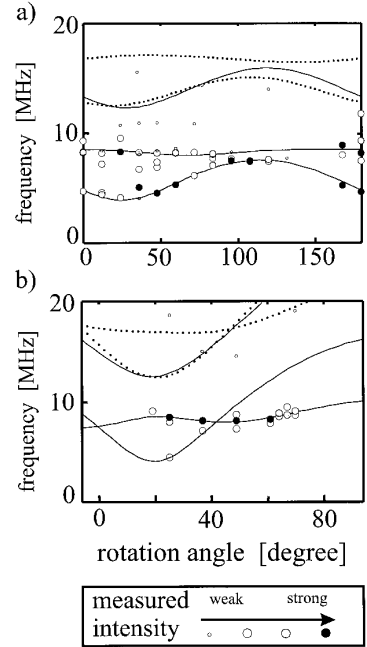


FIG. 4. Two ESEEM rotation patterns for independent rotation axes of a DANO crystal at 95 GHz; circles represent the measured frequencies with relative modulation intensities; simulations for the $m_s = -\frac{1}{2}$ and $m_s = +\frac{1}{2}$ subspaces are given by the solid and dotted lines, respectively. Experimental parameters: pulse length, $t_p = 100$ ns (120 ns); pulse spacing, $\tau = 250$ ns (290 ns) for spectrum a (b); stepping of pulse separation T in 20 ns increments; average of 300 echo signals for each data point for both spectra. Parameters for the simulation are the same as those in Fig. 3c. The tilting angle of the rotation axis against the molecular z -axis in the simulation is 9° (50°) for spectrum a (b), which corresponds to a rotational plane close to the xy -plane (diagonal through the hyperfine tensor). The high-frequency ESEEM lines are not observed experimentally because the B_1 field strength is too small.

The g -matrix anisotropy has been neglected because it is too small to cause observable effects on the ESEEM frequencies. A simplex minimization fit of the complete, amplitude-weighted data set without prefixed parameters turned out to be difficult: The energy surface for the parameter minimization is six-dimensional (A_{xx} , A_{yy} , Q_{zz} and three Euler angles for the rotation) and appeared to be highly complex with many narrow local minima. Instead, simulations with the same fixed parameters as those for the powder simulations were performed and tested for consistency with the chosen crystal orientations.

A single coupling tensor such as \tilde{A} would produce a frequency/angle dependence described by a sine function. In contrast to this (see Figs. 4a and 4b) the observed rotational shifts of the lines are deformed or flattened out. This can only be described by means of a second interaction tensor, which in our case is the quadrupole coupling \tilde{Q} . It can impose a dramatic effect on the mixing of spin eigenfunctions and consequently on the lineshape, especially when hyperfine and quadrupole couplings become similar in strength. The two lines with the strongest intensities in Fig. 4a could only be simulated within a narrow parameter range. The angles obtained from the simulation correspond very well with the alignment of the needle crystal in the experiment. The rotation

axis is tilted by an angle of 9° against the z -orientation, defining a rotational plane close to the molecular xy -plane. Using the same values of the parameters Q_{zz} , A_{xx} , and A_{yy} also for the simulation of the second independent rotation pattern (Fig. 4b) we obtained a tilting angle of 50° , in agreement with the experimental alignment of the plate crystals. In both pictures the experimental frequency positions are indicated by circles with different sizes and shadings to show their relative intensities. Calculated frequencies of the $m_s = -\frac{1}{2}$ and $m_s = +\frac{1}{2}$ subspaces are given by the solid and dotted lines, respectively. The values obtained for the hyperfine tensor \tilde{A} and the quadrupole tensor \tilde{Q} are listed in Table 1. Assuming a symmetric quadrupole tensor ($\eta = 0$), Q_{zz} is determined to be 3 MHz within rather narrow limits. Other, weaker lines showing up in the rotation patterns are attributed to crystal imperfections and to signals arising from radical pairs in neighboring crystal sites (17). The parameters obtained from the crystal simulations convincingly confirm the results obtained from the powder simulation. The ability to obtain such specific information about ^{14}N couplings independently from powder and crystal measurements is, in the case of DANO, supported by the strong anisotropy of the nitrogen hyperfine tensor.

CONCLUSION

We have shown that ESEEM measurements of nitrogen couplings are possible even at mw frequencies as high as 95 GHz. Because the magnetic field is higher by a factor of 10 relative to standard X -band spectrometers the nitrogen couplings show up selectively, because other nuclear couplings such as those from protons can no longer be detected. Therefore the ESEEM spectra become much easier to analyze. Most nitroxide radicals show a rather large anisotropy of both g -matrix and hyperfine tensor. While hyperfine anisotropy is a major precondition to see ESEEM at all, g -matrix anisotropy can be used to gain higher spectral resolution in disordered systems. This is achieved by separating different orientations with respect to the magnetic field axis, thereby providing crystal-like information. We were thus able to determine A_{xx} and A_{yy} as well as Q_{zz} from the 2D ESEEM powder spectrum. The results are consistent with single-crystal measurements performed at W -band frequencies. The results demonstrate that W -band ESEEM or ENDOR experiments are useful tools for investigating nitrogen couplings ($^{14}\text{N}/^{15}\text{N}$) in disordered systems, as, for example photosynthetic reaction centers or other protein complexes and enzymes.

ACKNOWLEDGMENTS

We thank Professor Carlo Corvaja, University of Padua, for the DANO crystals and their respective crystal structures, and Dr. Jens Törring and Dr.

Martin Rohrer for experimental assistance with the first ENDOR and ESEEM experiments. This work was supported by the Deutsche Forschungsgemeinschaft (SFB 337), which is gratefully acknowledged.

REFERENCES

1. G. Feher, *Phys. Rev.* **103**, 834 (1956).
2. W. B. Mims, *Proc. R. Soc. London* **283**, 452 (1965).
3. E. R. Davies, *Phys. Lett. A* **47**, No. 1 (1974).
4. W. B. Mims, in "Electron Paramagnetic Resonance," (S. Geschwind, Ed.), Plenum, New York (1972).
5. S. A. Dikanov, and Yu. D. Tsvetkov, in "Electron Spin Echo Envelope Modulation Spectroscopy," CRC Press, Boca Raton, FL (1992).
6. D. E. Budil, K. A. Earle, W. B. Lynch, and J. H. Freed, in "Advanced EPR in Biology and Chemistry," (A. J. Hoff, Ed.), Elsevier, Amsterdam/New York (1989).
7. Ya. S. Lebedev, O. Ya. Grindberg, A. A. Dubinskii, and O. G. Poluektov, in "Bioactive Spin Labels," (R. Zhdanov, Ed.), Springer-Verlag, Berlin/New York (1992).
8. Yu. D. Tsvetkov, V. I. Gulín, S. A. Dikanov, and I. A. Grigor'ev, in "Electronic Magnetic Resonance of Solid State," (J. A. Wail, M. K. Bowman, J. R. Morton, and K. F. Preston, Eds.), Canadian Society of Chemistry (1987).
9. H. L. Flanagan, and D. J. Singel, *J. Chem. Phys.* **87**, 5606 (1987).
10. P. Höfer, A. Grupp, H. Nebenführ, and M. Mehring, *Chem. Phys. Lett.* **132**, 279 (1986).
11. A. Schweiger, in "Modern Pulsed and Continuous-Wave Electron Spin Resonance," (L. Kevan and M. Bowman, Eds.), Wiley, New York (1990).
12. J. W. A. Coremans, M. van Gastel, O. G. Poluektov, E. J. J. Groenen, T. den Blaauwen, G. van Pouderoyen, G. W. Canters, H. Nar, C. Hamman, and A. Messerschmidt, *Chem. Phys. Lett.* **235**, 202 (1995).
13. T. F. Prisner, in "Advances in Magnetic and Optical Resonance," (W. W. Warren, Ed.), Vol. 20, 245, Academic Press (1997).
14. T. F. Prisner, M. Rohrer, and K. Möbius, *Appl. Magn. Reson.* **7**, 167 (1994).
15. L. R. Becerra, G. J. Gerfen, B. F. Bellew, J. A. Bryant, D. A. Hall, S. J. Inati, R. T. Weber, S. Un, T. Prisner, A. E. McDermott, K. W. Fishbein, K. E. Kreisler, R. J. Tempkin, D. J. Singel, and R. G. Griffin, *J. Magn. Reson. A* **117**, 28 (1995).
16. O. Burghaus, M. Rohrer, T. Götzinger, M. Plato, and K. Möbius, *Meas. Sci. Technol.* **3**, 765 (1992).
17. O. Takizawa, *Bull. Chem. Soc. Jpn.* **46**, 1991 (1973).
18. C. Gemperle, A. Schweiger, and R. Ernst, *J. Magn. Reson.* **91**, 273 (1991).
19. W. B. Mims, *Phys. Rev.* **B 5**, 2409 (1972).
20. S. A. Dikanov, A. A. Shubin, and V. N. Parmon, *J. Magn. Reson.* **42**, 474 (1981).